JGR Space Physics

RESEARCH ARTICLE
10.1029/2022JA031199

# Wave and Particle Analysis of Z-Mode and O-Mode Emission in the Jovian Inner Magnetosphere

**J. D. Menietti**[1], **P. H. Yoon**[2], **T. F. Averkamp**[1], **W. S. Kurth**[1], **J. B. Faden**[1], **F. Allegrini**[3,4], **P. Kollmann**[5], **and S. J. Bolton**[3]

[1]Department of Physics and Astronomy, University of Iowa, Iowa City, IA, USA, [2]Institute for Physical Science and Technology, University of Maryland, College Park, MD, USA, [3]Southwest Research Institute, San Antonio, TX, USA, [4]Physics and Astronomy Department, University of Texas at San Antonio, San Antonio, TX, USA, [5]Applied Physics Laboratory, The Johns Hopkins University, Laurel, MD, USA

**Key Points:**

- Intense Z-mode and O-mode in the Jovian inner magnetosphere yield important plasma parameters
- Direction finding suggests that each mode is from a different source region
- Quasilinear wave analysis of in-situ phase space density provides wave growth temporal development

**Correspondence to:**

J. D. Menietti,
john-menietti@uiowa.edu

**Citation:**

Menietti, J. D., Yoon, P. H., Averkamp, T. F., Kurth, W. S., Faden, J. B., Allegrini, F., et al. (2023). Wave and particle analysis of Z-mode and O-mode emission in the Jovian inner magnetosphere. *Journal of Geophysical Research: Space Physics*, *128*, e2022JA031199. https://doi.org/10.1029/2022JA031199

Received 30 NOV 2022
Accepted 17 APR 2023

**Abstract** We report some of the most intense Z-mode and O-mode observations obtained by the Juno spacecraft while in orbit about Jupiter in a low to mid-latitude region near the inner edge of the Io torus. We have been able to estimate the density of the plasma in this region based on the lower frequency cutoff of the observed Z-mode emission. The results are compatible with the electron density measurements of the Jovian Auroral Distributions Experiment (JADE), on board the Juno spacecraft, if we account for unmeasured cold plasma. Direction-finding measurements indicate that the Z- and O-mode emission have distinct source regions. We have also used the measured phase space density of the JADE and the Jupiter energetic particle detector instruments to calculate estimated local growth rates of the observed O-mode and Z-mode emission assuming a loss cone instability and quasilinear analysis. The results suggest the emissions were observed near, but not within, a source region, and the free energy source is consistent with a loss cone. We have thus carried out the quasilinear wave analysis of the assumed remote Z- and O-mode wave growths. It is shown that the remotely generated waves, propagated through an inhomogeneous medium to the satellite location, may account for the observed wave characteristics. The importance of Z-mode in accelerating electrons in the inner Jovian magnetosphere makes these new wave mode confirmations at Jupiter of particular interest.

## 1. Introduction

Broadband and narrowband kilometric radio emissions at Jupiter (bKOM and nKOM) have been studied extensively since the Voyager mission. bKOM is typically bursty and extends over frequencies from 10 kHz to 1 MHz. It is observed in both extraordinary and ordinary modes and is believed to have sources located in the dayside high latitude region of Jupiter's magnetosphere. nKOM is relatively weaker with peak intensities near 100 kHz. These emissions are believed to have a source near the outer and perhaps inner edges of the plasma torus, and display a periodicity that is somewhat slower than the Jovian rotation rate (Carr et al., 1983). nKOM is observed in both ordinary (O-) and extraordinary (X- and Z-) modes. O-mode is left-hand polarized and X-mode is right-hand polarized, but Z-mode can have either polarization dependent on the ratio of plasma frequency to cyclotron frequency. The Z-mode is a lower frequency branch of the extraordinary mode (Melrose, 1986).

Z-mode emission, the low-frequency branch of the extraordinary (X) mode, is observed at Jupiter in the inner magnetosphere at mid latitudes. Z-mode propagates below the upper hybrid frequency (or more precisely, the Z-mode resonance frequency $f_Z^{\mathrm{res}}$) and above the lower cutoff frequency, $f_Z$, hence, the Z-mode frequency range is defined by $f_Z < f < f_Z^{\mathrm{res}}$, where

$$
\begin{aligned}
f_Z &= \frac{f_{ce}}{2}\left[\left(1+\frac{4f_{pe}^2}{f_{ce}^2}\right)^{\frac{1}{2}}-1\right],\\
f_Z^{\mathrm{res}} &= \frac{f_{ce}}{2^{\frac{1}{2}}}\left\{\frac{f_{uh}^2}{f_{ce}^2}+\left[\left(1-\frac{f_{pe}^2}{f_{ce}^2}\right)^2+\frac{4f_{pe}^2}{f_{ce}^2}\sin^2\theta\right]^{\frac{1}{2}}\right\}^{\frac{1}{2}}.
\end{aligned}
\tag{1}
$$

Here, $f_{pe} = \omega_{pe}/(2\pi)$ and $f_{ce} = \Omega_{ce}/(2\pi)$ represent the plasma frequency and electron gyro frequency, respectively, $\omega_{pe} = \left(4\pi n_0 e^2/m_e\right)^{\frac{1}{2}}$ and $\Omega_{ce} = eB_0/(m_e c)$ being the angular frequency counterparts. In Equation 1,

$f_{uh} = \left(f_{pe}^2 + f_{ce}^2\right)^{\frac{1}{2}}$ is the upper-hybrid frequency. Note that for $\theta = \pi/2$ the Z-mode resonance frequency becomes the upper-hybrid frequency. The various notations are standard, $e$, $c$, $m_e$, $n_0$, and $B_0$ denoting the unit electric charge, the speed of light, the electron mass, ambient plasma density, and the background magnetic field intensity, respectively.

At Jupiter, the Z-mode emission is generally less intense and is usually observed at higher frequencies than whistler mode. Z-mode emission is observed at mid latitudes near the inner edge of the Enceladus plasma torus at Saturn, and at mid latitudes and near the inner edge of the Io torus at Jupiter (Menietti et al., 2018, 2021). Z-mode waves can efficiently scatter electrons and thus induce a stochastic acceleration (Horne & Thorne, 1998; Woodfield et al., 2018; Yu et al., 2019). The region between Jupiter and the inner edge of the Io Torus contains magnetic field lines that map to the inner radiation belts, and hence contain very energetic electrons. The source of these energetic electrons is not completely known (Kollmann et al., 2018), and Z-mode may have a role in contributing to the acceleration process. To date the source region and generation mechanism for this emission at Jupiter have been elusive. Some preliminary studies have shown possible source mechanisms at Saturn, but the data have been sparse and not definitive, cf. Gu et al. (2013), Menietti et al. (2016, 2019).

In this study we present an example of intense Z-mode observed at Jupiter during one of the early Juno orbits that may be near a source region. We show electron phase space distributions from the Jovian Auroral Distributions Experiment (JADE) and the Jupiter energetic particle detector (JEDI) that suggest loss cones with possible (but not observed) field-aligned energetic electrons, which can be sources of Z-mode and O-mode emission at Jupiter. The broadband emission marked by black arrows in a later figure (specifically, Figure 2—see below) may be associated with field-aligned electron beams, but the particle detectors could not observe along $B$ at this time, so these beams are merely speculated. Unfortunately, the field-aligned direction was only approached within about 5° and 15° by JEDI and JADE, respectively, and assumptions must be made when modeling the electron distributions close to the field-aligned direction. We have used the measured phase space density (PSD) of the JADE and JEDI instruments to calculate estimated local growth rates of the observed O-mode and Z-mode emission assuming a loss cone. The results suggest, however, that the observed emission characteristics are not consistent with local instability growth rates, which leads us to conclude that the emissions were observed near, but not within, a source region. We have thus further performed the quasilinear wave analysis of Z- and O-mode wave growths of the assumed remote source regions. Based upon the quasilinear calculation of the remote generation of these waves, and upon implementing the basic scheme to model the wave propagation in inhomogeneous medium, it is shown that the theoretical model may account for the observed wave characteristics.

## 2. Juno Fields and Particle Instruments

The Juno Waves instrument (Kurth et al., 2017) measures electric signals in the frequency range ∼10–∼150 kHz on the low frequency receiver (LFR-hi), ∼50 Hz–20 kHz on LFR-lo, and magnetic signals in the range ∼50 Hz–20 kHz on the LFR-B receiver. The high frequency receiver (HFR-lo) measures electric signals in the range 100 kHz–3 MHz, and is used in this study to indicate the local cyclotron frequency. In the survey mode used in this study, spectra are returned about once every second. The instrument also operates in a burst mode with greater spectral resolution. While in burst mode, the instrument can monitor frequencies close to $f_{ce}$ and survey at the rate of 1 spectrum/sec to frequencies up to 41 MHz. Because of the single dipole antenna of the Waves instrument, no polarization measurements are possible.

The JEDI consists of three almost identical instruments that measure spectra and pitch angle distributions of electrons and ions (Mauk et al., 2017). In this study, we will focus on electron distributions that are measured over an energy range of about 25–800 keV. Sampling time for the energy range of electrons is 0.5 s.

The JADE measures energetic electron and ion spectra over a broad energy range (Allegrini et al., 2017, 2020; McComas et al., 2017). Electrons are measured with top-hat electrostatic analyzers ∼50 eV–∼100 keV. A full energy spectrum is possible every 1 s with a 10%–14% resolution. Pitch angles are averaged over all energies and are calculated every 1 s with a resolution of ∼7.5° in azimuth (Juno spin plane) and ∼2°–6° in elevation. The spin rate of the Juno spacecraft is about 30 s.

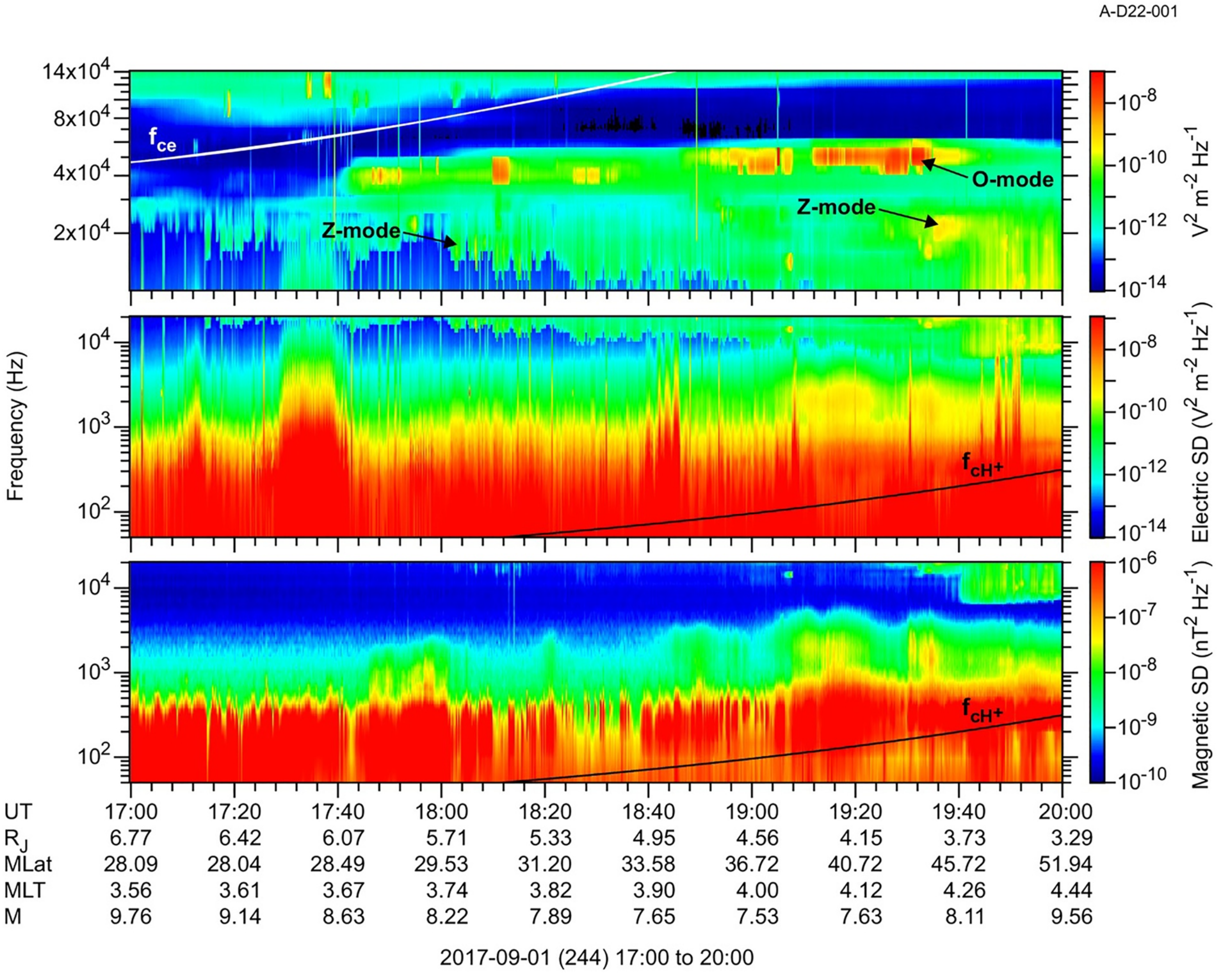

**Figure 1.** A frequency-time spectrogram of Juno Waves data. Top panel: Electric antenna wave spectral density (SD) from 10 to 140 kHz; Middle panel: Electric SD from 50 Hz to 20 kHz; Bottom panel: Magnetic SD from 50 Hz to 20 kHz. The black line ($f_{cH+}$) designates the proton cyclotron frequency.

## 3. Observations

In Figure 1 we present a frequency-time spectrogram of Juno Waves data. In the top panel we plot electric wave spectral density (SD) in the frequency range 10–140 kHz from the LFR-hi receiver. The middle panel contains the electric wave SD from 50 Hz to 20 kHz, while the bottom panel displays the magnetic wave SD in the same frequency range. The intensity of the Z-mode and O-mode emission observed at this time is near the highest observed by Juno Waves. These observations occur over an approximate range of M-shells—cf. Connerney et al. (2018), $7.5 < M < 9.5$ and magnetic latitudes (based on JMR09 (Connerney et al., 2018)) in the range $28.5° < \lambda < 52°$, and over the approximate radial distance range of $3.2 < r/R_J < 6$ ($1\ R_J = 71{,}492$ km). This is near and outside the inner edge of the Io plasma torus in a region where the ratio of electron plasma to cyclotron frequency, $f_{pe}/f_{ce} < 1$. This orbit of the Juno spacecraft (PJ08) appears to have a high rate of plasma injections, which are regions of energy dispersing electrons and/or convective magnetic flux tube interchange—cf. Mauk et al. (1999), Thorne et al. (1997), Bolton et al. (1997).

In Figure 2 we focus on a subset of the data from the top two panels of Figure 1. The top panel displays the Waves electric field spectral densities over an expanded frequency range (5–800 kHz) from the LFR-hi and HFR in order to include the electron cyclotron frequency, $f_{ce}$. The lower panel is from LFR-lo over the frequency range 50 Hz–20 kHz. We over-plot the spectrogram with several lines. We show a white line near the lower cutoff of what we identify as Z-mode emission, $f_z$ (Equation 1). Assuming this is a correct identification of Z-mode we can then calculate the expected value of $f_{pe}$ to be

$$f_{pe} = [f_Z(f_Z + f_{ce})]^{1/2}. \tag{2}$$

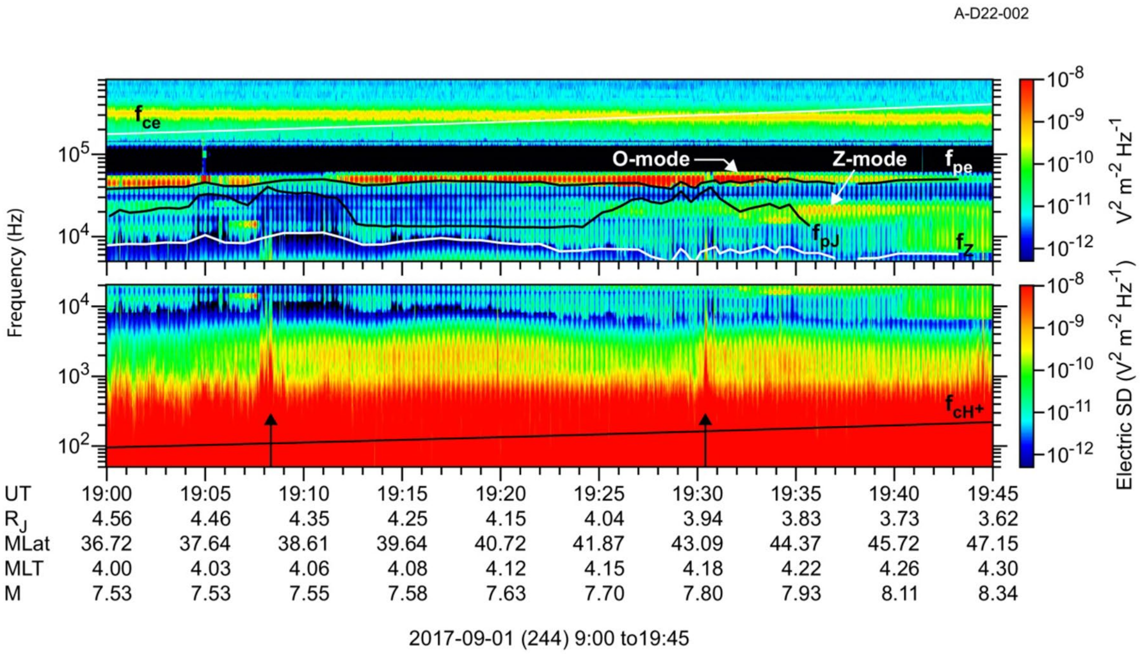

**Figure 2.** A subset of the data from the top two panels of Figure 1. Top panel: Electric spectral density (SD) for an expanded frequency range (5–800 kHz) including the electron cyclotron frequency, $f_{ce}$; Lower panel: Electric SD, 50Hz–20 kHz. Over-plotted lines: White line near the lower cutoff of what we identify as Z-mode emission ($f_Z$); Upper black line is the estimated value of $f_{pe}$ based on the identification of $f_Z$; Lower black line is the plasma frequency ($f_{pJ}$) determined from the electron density obtained from Jovian Auroral Distributions Experiment.

The upper black line is then the estimated value of $f_{pe}$ (proportional to $\sqrt{n_e}$) based on the identification of Z-mode and $f_Z$, and we note that it lies quite close to the lower frequency limit of the more intense, narrow band emission between about 40 and 50 kHz. We believe this most intense (red color) emission is ordinary mode (O-mode), which has a low-frequency cutoff at the plasma frequency. Similar procedures for identifying emission signatures at Jupiter have been demonstrated by Menietti et al. (2021), Sulaiman et al. (2021), Elliot et al. (2021). Note also that the intense red emission intensity fades and the lower frequency cutoff increases at times when $f_{pe}$ increases (such as 19:08 to 19:12), indicating that it is probably a mixture of O-mode and Z-mode, since the Z-mode does not cutoff at $f_{pe}$ and can extend to higher frequency. Dropouts in the intense emissions occur near and above ~40 kHz when there are density increases seen near 19:05–19:06, 19:08–19:11 and near 19:30–19:31. The Z-mode emission lower frequency cutoff during these times is dependent on both $f_{pe}$ and $f_{ce}$, and ranges from ~10 kHz between 19:08–19:11 down to ~5 kHz for the range ~19:28–~19:29, for instance.

In Figure 2, top panel, we also over-plot the plasma frequency determined from the electron density obtained from JADE (indicated as $f_{pJ}$). These densities do not account for the cold plasma ($E < 50$ eV) which is not measured by JADE, but they are nevertheless informative. When density values measured by JADE reach a peak there is a corresponding increase in the upper frequency of electrostatic emissions observed by the Waves instrument as shown in the lower panel of Figure 2 for the time ranges ~19:07:30–19:08:30 and ~19:30–19:31 (near the black arrows shown in the lower panel). These broad band emissions may be associated with electron bursts. Broadband electrostatic emission is commonly observed associated with electron beams—cf. Gurnett and Frank (1972). The 30-s averaged density measured by JADE during these times increases by over 10 cm$^{-3}$. However, field-aligned electron beams are not visible by JADE because pitch angles less than ~15° are not sampled by JADE at this time.

## 4. Electron Phase-Space Distributions

We focus on the time near 19:31:15 where emission in the frequency range 40 kHz $< f <$ 50 kHz is intense and where we observe an increase in density associated with an electrostatic burst seen in lower panel of Figure 2. Figures 3a and 3b are contour plots of the JADE and JEDI PSD, respectively. These data are 30-s averages with a resolution in pitch angle of ~7.5° for the JADE data, and approximately 10° for the JEDI data. The kinetic energies of the detectors have been corrected for relativistic effects. For JEDI, energy steps less than ~25 keV

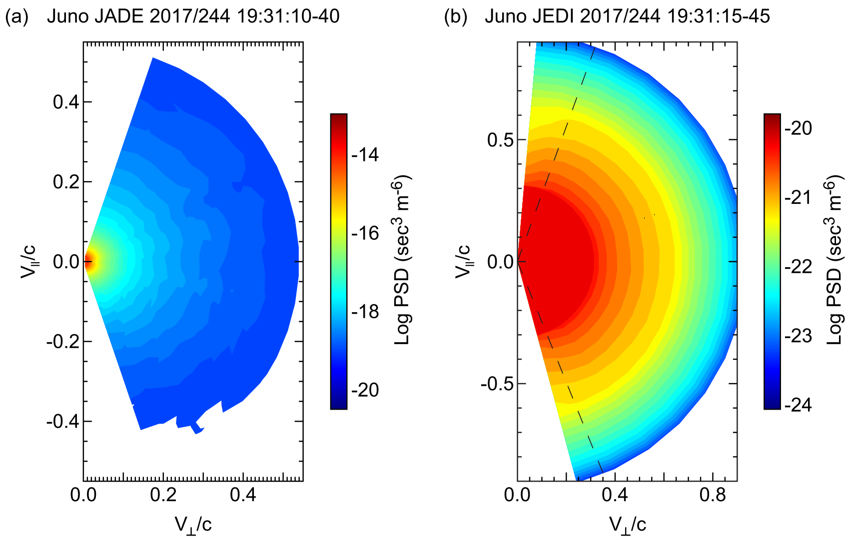

**Figure 3.** Contour plots of the Jovian Auroral Distributions Experiment (a) and Jupiter energetic particle detector (JEDI) (b) phase space density centered near 19:31:30 (O-mode). There is evidence of a loss cone beginning near 20° and 165° pitch angle in the JEDI data.

($v/c = 0.316$) are not as reliably accurate as the higher energy channels and have been set at a constant high value $\log_{10}(\mathrm{PSD}) = -19.8$ (dark red). We see evidence of a loss cone beginning near 20° and 165° pitch angle in the JEDI data. In order to conduct an analysis of these data, we have combined both sets of data by using JADE PSD for $E < 26$ keV, and JEDI PSD for 27 keV $< E <$ 974 keV. The combined distribution shows a smooth transition from JADE to JEDI as will be shown below.

We model the combined distributions using a sum of bi-Maxwellians—cf. Menietti et al. (2016). Thus, $f = \sum f_s$, and

$$f_s = \frac{n_e^s}{\pi^{3/2} w_{\perp s}^2 w_{\parallel s}} \frac{(1-\Delta_s)\beta_s - \Delta_s}{\beta_s} \exp\left(-\frac{v_\perp^2}{w_{\perp s}^2} - \frac{(v_\parallel - v_{ds})^2}{w_{\parallel s}^2}\right). \tag{3}$$

Here, $v_\perp$ and $v_\parallel$ are velocity components perpendicular and parallel with respect to the direction of the ambient magnetic field vector. We have performed a nonlinear least-squares fit of these data to a sum of five bi-Maxwellians—see, for example, Equation 1 in Menietti et al. (2016)—where $w_\parallel$ and $w_\perp$ are the parallel and perpendicular thermal speeds and $v_d$ is the drift velocity (=0 in our case). The variable fit parameters are density $n_e$, $w$, and $T_\perp/T_\parallel$ for each population. In addition, $\Delta$ and $\beta$ are the loss cone parameters for depth and width, respectively. The fitting routine uses a gradient expansion algorithm—cf. Bevington (1969)—to compute a nonlinear least squares fit to a user-supplied function with known partial derivatives. The goodness-of-fit statistic, $\chi^2$, is weighted by the standard deviation. We use multiple (Equation 5) bi-Maxwellians to increase the ability to model rapid changes as a function of energy and pitch angle.

The best fitting parameters are listed in Table 1. The sum of the plasma populations in the table totals 10.63 cm$^{-3}$, but is missing the cold plasma population not measured by JADE or JEDI. Based on the analysis above that the dominant emission is O-mode with a low-frequency cutoff at the plasma frequency shown in Figure 2 by the black line labeled "$f_{pe}$", we estimate $f_{pe} = 43.5$ kHz at this time, or $n_e \sim 23.5$ cm$^{-3}$ and $f_{pe}/f_{ce} = 0.142$. In Figure 4 we show labeled line contours of the observed distribution (a) and the fitted distribution (b) for the combined JADE and JEDI data of Figures 3a and 3b, which provide a visual display of the goodness of fit. For these data $\chi^2 = 47.8$. We have enhanced the size of the loss cone assuming the observed loss cone has undergone filling due to the instrument sampling time.

**Table 1**
*Distribution Fitting Parameters for Sum of 4 Bi-Maxwellians With Loss Cone (O-Mode Near 19:31:10–45)*

| $n_s$ (m$^{-3}$) | $w_{\parallel s}$ (m/s) | $w_{\perp s}^2/w_{\parallel s}^2$ | $\Delta_s$ | $\beta_s$ |
|---|---|---|---|---|
| $9.46 \times 10^6$ | $4.43 \times 10^6$ | 1.03 | 0.1 | 0.2 |
| $9.09 \times 10^5$ | $1.21 \times 10^7$ | 1.10 | 0.2 | 0.4 |
| $6.49 \times 10^3$ | $6.33 \times 10^7$ | 0.00555 | 0.9 | 0.9 |
| $1.45 \times 10^5$ | $3.36 \times 10^7$ | 0.565 | 1.0 | 0.9 |
| $1.14 \times 10^5$ | $8.14 \times 10^7$ | 0.552 | 1.0 | 0.9 |

Z-mode emission reaches a local peak in intensity in the range from approximately 19:33 to 19:40, in the approximate frequency range 13 kHz $< f <$ 28 kHz as seen in Figure 2. We show contours of the combined

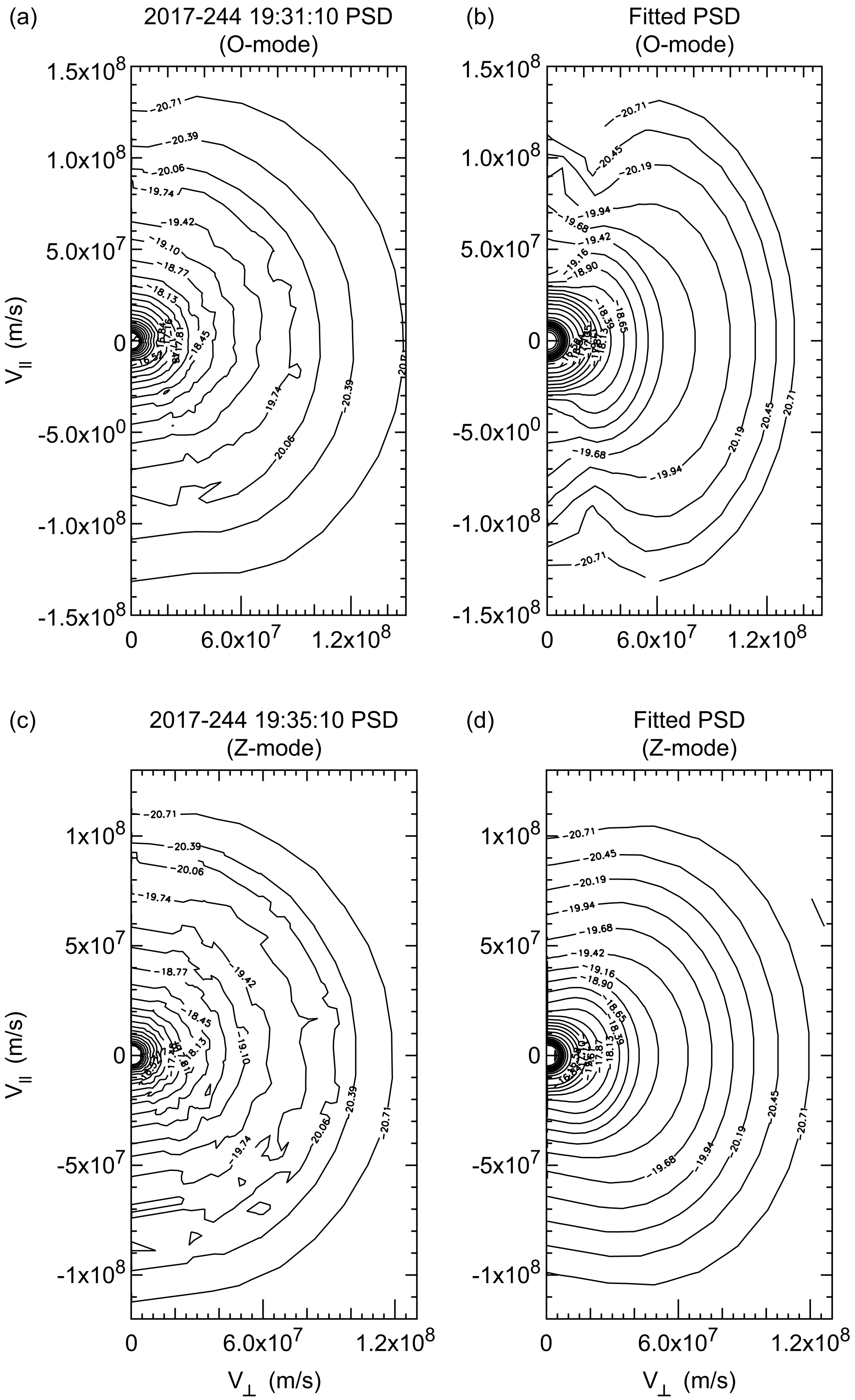

**Figure 4.** (a) Labeled contour plot of the observed O-mode electron phase space distribution of Figure 3 (19:31:10). (b) The five bi-Maxwellian fit for the observed O-mode of 4a. (c) Labeled contour plot of the observed electron phase space distribution of Figure 5 (19:35:10). (d) The five bi-Maxwellian fit for the observed Z-mode of Figure 5.

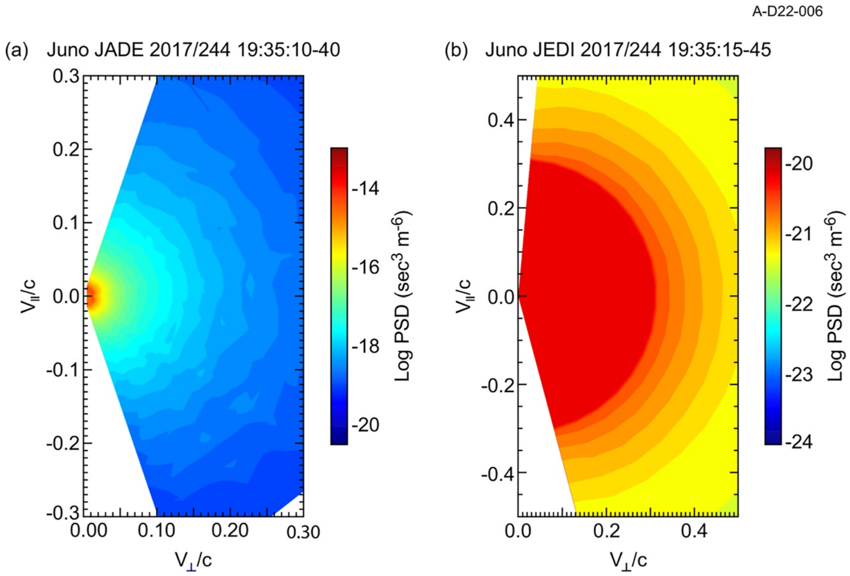

**Figure 5.** Contour plots of the Jovian Auroral Distributions Experiment (a) and Jupiter energetic particle detector (b) phase space density centered near 19:35:30 (Z-mode).

JADE and JEDI electron PSD centered near 19:35:30 in Figures 5a and 5b, respectively. The JADE instrument observations do not get closer than about 15° to the magnetic field line direction, whereas the JEDI instrument is closer, ~5°. The JADE data therefore show only a suggestion of a loss cone, whereas the JEDI data indicate a weak loss cone above 25 keV (the JEDI data for $E < 25$ keV being not as reliable). As before, we have combined the two data sets and performed a nonlinear least-squares fit to a sum of 5 bi-Maxwellian plasma distributions. The fitting parameters for the combined JADE and JEDI electron phase space distributions are shown in Table 2.

The sum of the plasma populations in the table totals 6.62 cm$^{-3}$, not including the cold plasma population. We correct for this again by estimating the O-mode low-frequency cutoff at the plasma frequency shown in Figure 2 to be $f_{pe} = 41.5$ kHz at this time, or $n_e \sim 21.4$ cm$^{-3}$ and $f_{pe}/f_{ce} = 0.124$. Figures 4c and 4d show labeled line contours of the combined observed plasma distribution (c) and the fitted combined distribution (d), respectively. $\chi^2 = 32.9$ for the fitted data.

## 5. Remote Generation of Z- and O-Modes and Propagation Through Inhomogeneous Medium to Local Observation Sites

As discussed by Menietti et al. (2019) (cf. Yoon et al., 1998), the electron distribution function is assumed to be made of a background of relatively cold electrons and an energetic population of loss-cone distributed electrons. The free energy for wave instability comes from the effective temperature anisotropy provided by the loss cone. Energetic electrons trapped within Jupiter's magnetosphere naturally form a loss-cone feature. Once a wave instability is excited, we expect the empty loss cone to be filled, removing the source of instability and forming a relaxed distribution. Thus, we expect that the most important factor in the time evolution of the distribution function in response to the wave excitation is loss-cone filling by pitch-angle diffusion.

**Table 2**
*Distribution Fitting Parameters for Sum of 5 Bi-Maxwellians With Loss Cone (Z-Mode Near 19:35:10–45)*

| $n_s$ (m$^{-3}$) | $w_{\|s}$ (m/s) | $T_{\perp s}/T_{\|s}$ | $\Delta_s$ | $\beta_s$ |
|---|---|---|---|---|
| $5.25 \times 10^6$ | $3.26 \times 10^6$ | 1.10 | 0.1 | 0.2 |
| $6.63 \times 10^5$ | $7.52 \times 10^6$ | 1.18 | 0.2 | 0.4 |
| $1.64 \times 10^5$ | $1.97 \times 10^7$ | 0.742 | 0.7 | 0.9 |
| $8.91 \times 10^4$ | $4.68 \times 10^7$ | 0.753 | 0.7 | 0.9 |
| $3.48 \times 10^4$ | $1.04 \times 10^8$ | 0.552 | 0.7 | 0.9 |

With these premises, we model a presumed "initial" electron distribution function before it relaxes due to quasilinear relaxation. As noted, one may characterize the five bi-Maxwellian model (Equation 3) with a weak signature for the loss cone, at least in the case when O-mode is dominant. In modeling the initial state of the electrons we slightly enhance the presumed loss cone. We model the electron distribution by a sum of an isotropic Maxwellian background characterized as a relatively cold component (which supports the waves) and a more energetic loss-cone component, which supports the wave growths. The hot component $f_h$ is modeled by (Menietti et al., 2016; Yoon et al., 1998)

$$\begin{aligned} f_h &= \frac{n_h}{\pi^{3/2}\alpha_h^3(A+\Delta)}\exp\left(-\frac{u^2}{\alpha_h^2}\right)\left(\tanh\frac{\mu+\mu_L}{\delta}-\tanh\frac{\mu-\mu_L}{\delta}+\Delta\right), \\ A &= \frac{1}{2}\int_{-1}^{1} d\mu\left(\tanh\frac{\mu+\mu_L}{\delta}-\tanh\frac{\mu-\mu_L}{\delta}\right), \end{aligned} \tag{4}$$

where $u = v/c$, $\mu = u_\parallel/u$, $u = \left(u_\perp^2 + u_\parallel^2\right)^{\frac{1}{2}}$; $\alpha_h$ denotes the normalized thermal speed associated with the hot loss-cone component; $\mu_L$ is cosine of the loss-cone angle; $\delta$ signifies the smoothness of the loss-cone boundary; and $\Delta$ determines the depth of the loss-cone, or equivalently, the loss-cone filling factor. As noted, the loss-cone filling by pitch-angle diffusion is expected to be the most important factor in the time evolution, so in the subsequent quasilinear analysis, we hold other parameters fixed, while $\Delta$ is allowed to vary in time. The parameter $\Delta$, which is set equal to zero for the initial state, will thus be calculated self-consistently at each time step together with the wave spectrum evolution. For $\Delta \gg 1$, the loss-cone model reduces to the isotropic thermal distribution. For the subsequent analysis we adopt the following choice for input parameters: $n_h/n_0 = 10^{-3}$, where $n_0$ denotes the background electron density, $\alpha_h = 0.3$, $\mu_L = 0.95$ (corresponding to $\sim\mathcal{O}(10^\circ)$ loss-cone angle), $\delta = 0.1$.

Note that these values are somewhat arbitrary as they relate to the hypothetical source regions for which, direct observations are not available. Based on Tables 1 and 2, on the other hand, the ratio of hot-to-background electron densities at the satellite location appears to be significantly higher than $n_h/n_0 = 10^{-3}$ by at least a factor of 2–3. At the presumed source region, we chose a somewhat lower value of $n_h/n_0 = 10^{-3}$. The hot electron density ratio, $n_h/n_0$, as well as the normalized hot electron thermal speed, $\alpha_h$, the loss-cone angle, $\mu_L$, and the loss-cone edge smoothing factor, $\delta$, are all somewhat arbitrary, and we could have made different choices for these parameters. In our recent paper (Yoon et al., 2021), where we carried out the quasilinear wave analysis for the whistler chorus mode emission, which is similar to the present Z- and O-mode analysis in terms of technical aspects, we have indeed made a systematic variation of modeling parameters such as those adopted in the present study. We have found that, while the variations of the modeling parameters do have quantitative influences on the outcome, they do not qualitatively change the overall result. We have carried out numerical studies by varying the input parameters, but the results are not shown for the sake of brevity. Instead, in what follows, we will discuss only samples cases. However, in this regard, a recent similar analysis involving the Jovian whistler mode emission does provide the results of parametric study (Yoon et al., 2021). For this reason, we do not repeat the parametric variations in the electrons model in the present paper.

We conduct a quasilinear analysis similar to that of Yoon et al. (2021), except in the present case, we must deal with the O-mode emission in addition to the Z-mode excitation. As the Z-mode near the upper-hybrid frequency a sub-luminal mode ($ck > \omega$), the non-relativistic formalism adopted in Yoon et al. (2021) is applicable. However, the O-mode, which is a super-luminal mode ($ck < \omega$), the non-relativistic formalism is inapplicable. Consequently, we adopt the weakly relativistic formalism for quasilinear time development of both modes (Yoon & Ziebell, 1995; Ziebell & Yoon, 1995). The energetic electrons could undergo a mild heating or cooling in response to wave mode excitation, but we expect that the most important dynamical change will be associated with the loss-cone filling factor $\Delta$, which controls the degree of emptiness associated with the loss cone distribution. This is because the relativistic cyclotron resonance condition predominantly leads to the pitch-angle diffusion in momentum space, while the diffusion in energy space is the next-order process. This is well known in the theory of radiation belt quasilinear transport theory, for instance (Lyons et al., 1972). The primary effect of pitch-angle diffusion is to erode the loss-cone boundary, and thus fill up the empty loss cone. Initially, this parameter is set equal to zero, as noted, but as the wave instability is excited and proceeds toward saturation, we self-consistently calculate the time variation of $\Delta$ so that this parameter will increase from the initial value of zero to a finite value.

In agreement with the plasma parameters observed in Figure 2, we consider the range $0.1 < f_{pe}/f_{ce} < 0.3$ and an idealized initial loss cone extending to $\sim 12^\circ$ pitch angle is hypothesized. This loss cone is more enhanced than the observed distribution of Figure 3. The linear growth rate calculations carried out over the five bi-Maxwellian model indicate that the observed waves are not generated locally. In particular, the wave growth for O-mode approaches $\gamma/\Omega_{ce} \sim 7.5 \times 10^{-4}$, for $1.02 < \omega/\Omega_{ce} < 1.04$, which is well above the frequency range of the observed

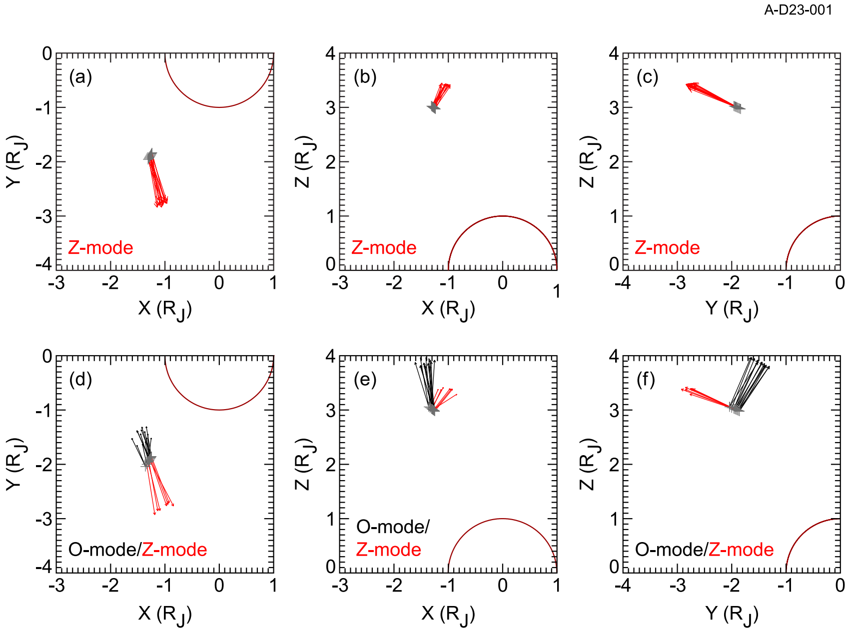

**Figure 6.** Direction finding for the Z-mode source regions (a–c) and for the O-mode regions (d–f). The coordinate axes are defined as follows: "*X*" is in the Jupiter-Sun plane, positive toward the sun; "*Y*" is $Z \times X$; "*Z*" is the northward spin axis of Jupiter.

O-mode (Figure 2). Likewise, an initial linear growth rate analysis for the Z-mode with a similar ratio of $0.1 < f_{pe}/f_{ce} < 0.3$ and an enhanced loss cone compared to Figure 4 yields wave growth for Z-mode that approaches $\gamma/\Omega_{ce} = 1 \times 10^{-4}$ for $1.003 < \omega/\Omega_{ce} < 1.005$. This frequency range is much higher than the frequency range of the observed Z-mode (Figure 2). This finding suggests that we are observing a relaxed plasma population and the source regions of both O- and Z-mode emissions could be nearby but not local.

From the cyclotron resonance condition we find that the expected frequency range of the O-mode emission for the observed plasma distribution would be at much higher frequency than observed. As shown by Equation 5.42 of Treumann and Baumjohann (1997), the gyro resonance ellipse has a radius in velocity space given by

$$\frac{v_r}{c} = \sqrt{\frac{k_{\parallel}^2 c^2 - \omega^2 + l^2 \Omega_{ce}^2}{k_{\parallel}^2 c^2 + l^2 \Omega_{ce}^2}}, \tag{5}$$

with a center located along $v_{\parallel}$ at

$$v_{c\parallel} = \frac{\omega k_{\parallel} c}{k_{\parallel}^2 c^2 + l^2 \Omega_{ce}^2}. \tag{6}$$

Assuming cold plasma theory we can calculate the dispersion relation for O mode using, for instance, Equations 7 and 8 from Menietti et al. (2016). Since the index of refraction is given by $n = kc/\omega$ we calculate for $l = 1$ and the plasma parameters $f_{pe}$ and $f_{ce}$ above (O-mode) and a range of wave normal angles from ∼5° to ∼90° that $v_r/c > 2.97$. This would require velocities close to the speed of light and electron energies near and above MeV, which are much higher than those observed locally. This indicates that the observed O-mode emission is coming from a remote source rather than a local source.

The observed Z-mode is clearly bounded in frequency from below by $f_Z$, but its bandwidth is quite broad. For $f_{pe}/f_{ce} < 1$, as is the case presently, the Z-mode resonance frequency $f_Z^{\text{res}}$ is far higher than $f_{pe}$. However, for frequency close to $f_{pe}$ and above, the O-mode intensity is sufficiently high so that the Z-mode and O-mode emissions may overlap. In spite of this, Figure 2 clearly shows that Z-mode emission takes place over a wide frequency range.

We have conducted direction finding analysis of the O- and Z-mode emission based on the spin modulation of the wave intensity observed in the data. The analysis technique is described in some detail by Menietti et al. (2020). The calculated directions to the source region are displayed in Figure 6. Each figure

**Table 3**
*Estimated Source Locations for Z-Mode as Function of Time and Frequency Time*

| Time | $f$ (Hz) | $\Lambda_3$ (deg) | lat (deg) | $r(R)j$ |
|---|---|---|---|---|
| 19:33 | 44,860 | 35.55 | 37.98 | 7.02 |
| 19:35 | 15,870 | 24.5 | 35.9 | 9.95 |
| 19:35 | 19,970 | 26.96 | 36.8 | 9.21 |
| 19:35 | 25,080 | 27.2 | 36.99 | 8.48 |
| 19:35 | 28,200 | 27.4 | 38.1 | 8.21 |
| 19:37 | 15,870 | 25.49 | 35.9 | 9.89 |
| 19:37 | 22,340 | 24.8 | 37.9 | 8.90 |
| 19:37 | 25,080 | 30.5 | 36.8 | 8.50 |
| 19:37 | 28,200 | 29.3 | 35.9 | 8.11 |
| 19:37 | 44,860 | 23.7 | 37.2 | 6.98 |

*Note*. Λ3 = system III longitude

contains three planes in Jupiter solar equatorial coordinates (JSQ), which are defined in the figure caption. The location of Juno is shown with a gray cross ("+") at the tail of each arrow. The arrow indicates the calculated direction to the source region determined by averaging the spin modulation results for over 1 min. Each arrow represents a distinct frequency channel within the designated frequency range. Figures 6a–6c show the results for the Z-mode (19.97–22.3 kHz) as red arrows, and Figures 6d–6f displays the O-mode (50.2–56.2 kHz) as black arrows. In Figures 6d–6f we have also included a lower frequency channel at 44.9 kHz which lies close to but lower than $f_{pe}$. For this channel the wave intensities are lower than those of the O-mode emission above $f_{pe}$.

The length of each arrow is normalized to the same scale. Note that the source regions of the Z-mode (Figures 6a–6c) and O-mode (Figures 6d–6f) appear to be located at larger radial distances than the Juno spacecraft, hence in a region of lower magnetic field. Note also that red arrows in Figures 6d–6f represent emission at the lowest frequency channel (44.9 kHz) very near but below $f_{pe}$, and show a direction consistent with Z-mode (Figures 6a–6c). This is evidence that the Z-mode can extend in frequency near and above $f_{pe}$ (the low-frequency cutoff of O-mode). We surmise the O-mode emission is a mixture of O-mode and less intense Z-mode.

We have used the results displayed in Figure 6 to trace the calculated directions back to the source location. Assuming a gyroresonant wave generation mechanism as discussed below, within the source region the wave frequency will be close to the local (source region) cyclotron frequency. We assume the JMR09 magnetic field model for these tracings. For the Z-mode a source region is determined at a sample of times and frequencies shown in Table 3 (other times within the range 19:35–19:41 were similar). We have included the frequency 44.9 kHz in this table, consistent with its identification as Z-mode. The JSQ longitudes have been converted to system III longitudes ($\Lambda_3$).

The O-mode source region (Table 4) was found to be at similar distance, but higher latitude and outside the Io torus.

In order to explain the observation we have assumed separate remote sources for O- and Z-modes, and we have conducted separate quasilinear analysis for these waves, following the methods outlined in Yoon and Ziebell (1995), Ziebell and Yoon (1995). We will then implement a simple scheme to mimic the wave propagation in an inhomogeneous medium. The result, which will be discussed shortly, appears to provide a satisfactory explanation for the observation.

**Table 4**
*Estimated Source Locations for O-Mode as Function of Time and Frequency Time*

| Time | $f$ (Hz) | $\Lambda_3$ (deg) | lat (deg) | $r(R)j$ |
|---|---|---|---|---|
| 19:31 | 50.2 | 113.341 | 74.2 | 7.84 |
| 19:31 | 56.2 | 127.820 | 69.5 | 7.58 |
| 19:33 | 56.2 | 108.137 | 76.8 | 7.55 |
| 19:35 | 50.2 | 141.147 | 82.1 | 7.88 |
| 19:35 | 56.2 | 112.906 | 78.2 | 7.57 |
| 19:37 | 50.2 | 145.271 | 78.4 | 7.95 |
| 19:37 | 56.2 | 137.506 | 70.5 | 7.57 |

*Note*. $\Lambda_3$ = system III longitude

### 5.1. Quasilinear Analysis of O-Mode in the Source Region

The detailed theoretical development of quasilinear theory for cyclotron maser instability can be found in Yoon and Ziebell (1995), Ziebell and Yoon (1995). Consequently, we only present the essential mathematical formalisms for the sake of completeness but without derivation. In what follows, we assume that only the cyclotron harmonic, $l = 1$, participates in the wave-particle interaction, since $f_{pe}/f_{ce} = \omega_{pe}/\Omega_{ce} < 1$. The instantaneous growth rate for O-mode—under the assumption that the model hot electron loss-cone distribution function maintains its mathematical form except that $\Delta$ may change in time—can be summarized by the following dimensionless form:

$$
\begin{aligned}
& w=\frac{\omega}{\Omega_{ce}}, \qquad q=\frac{ck}{\Omega_{ce}}, \qquad r=\frac{\omega_{pe}}{\Omega_{ce}}=\frac{f_{pe}}{f_{ce}}, \qquad r_n=\frac{n_h}{n_0}, \\
& \Gamma=\frac{\gamma}{\Omega_{ce}}=\frac{\pi^{1/2}r_n r^2}{(A+\Delta)R}\Big(\Theta(1-w)\textstyle\int_{-1}^{1}d\mu\, Q(u_+,\mu) \\
& \quad +\Theta\big(1-\mu_*^2\big)\Theta(w-1)\textstyle\int_{\mu_*}^{1}d\mu\big(1-\mu^2\big)\sum\limits_{+,-}Q(u_\pm,\mu)\Big),
\end{aligned} \tag{7}
$$

where $\Theta(x)=1$, if $x>0$ and zero otherwise (the Heavyside step function), and various other quantities are defined by

$$
\begin{aligned}
u_\pm &= \frac{q\mu\cos\theta}{w}\pm\sqrt{\left(\frac{q\mu\cos\theta}{w}\right)^2+\frac{2(1-w)}{w}}, \qquad \mu_*=\frac{2w(w-1)}{q^2\cos^2\theta}, \\
Q(u,\mu) &= \frac{\big(1-\mu^2\big)\mathcal{M}(u,\mu)\mathcal{P}(u,\mu)}{4(\tau^2+\cos^2\theta)\Big|u\big[q^2\mu^2\cos^2\theta+2(w-1)w\big]^{1/2}\Big|}, \\
\mathcal{M}(u,\mu) &= \{[wK\sin\theta\cos\theta-\tau(w-qu\mu)][J_0(b)+J_2(b)]-\cos\theta[J_0(b)-J_2(b)]\}^2, \\
\mathcal{P}(u,\mu) &= \exp\left(-\frac{u^2}{\alpha^2}\right)\left[\frac{-2u^5}{\alpha^5}\left(\tanh\frac{\mu+\mu_L}{\delta}-\tanh\frac{\mu-\mu_L}{\delta}+\Delta\right)\right. \\
&\quad \left.+\frac{1}{\delta}\frac{u^3}{\alpha^3}\left(\frac{qu\cos\theta}{w}-\mu\right)\left(\tanh^2\frac{\mu-\mu_L}{\delta}-\tanh^2\frac{\mu+\mu_L}{\delta}\right)\right], \\
b &= qu\big(1-\mu^2\big)^{1/2}\sin\theta, \qquad s=\frac{w\sin^2\theta}{2|r^2-w^2|}, \qquad \tau=\left(s+\sqrt{s^2+\cos^2\theta}\right)\frac{r^2-w^2}{|r^2-w^2|}, \\
K &= \frac{r^2}{r^2-w^2}\frac{\tau\sin\theta}{\tau w-\cos^2\theta}, \qquad R=1+\frac{r^2}{w^2}\frac{\cos^2\theta}{\sin^2\theta}\frac{\tau^2r^2-w^2\cos^2\theta}{(\tau w-\cos^2\theta)^2}\frac{\tau^2-\cos^2\theta}{\tau^2+\cos^2\theta}.
\end{aligned} \tag{8}
$$

In Equation 8, $w$ and $\theta$ denote the normalized wave frequency for the O-mode and the wave propagation angle defined as the angle between the wave vector $\mathbf{k}$ and to the ambient magnetic field vector $\mathbf{B}_0$.

To determine the O-mode frequency $w$, we have numerically solved the cold-plasma (magnetoionic) dispersion relation,

$$
\begin{aligned}
0 &= q^4\big[w^2\big(w^2-1-r^2\sin^2\theta\big)-r^2\cos^2\theta\big(w^2-1\big)\big] \\
&\quad -q^2w^2\big[2\big(w^2-r^2\big)\big(x^2-1-r^2\big)-r^2\sin^2\theta\big] \\
&\quad +w^2\big(w^2-r^2\big)\big[w^2\big(w^2-1-2r^2\big)+r^4\big],
\end{aligned} \tag{9}
$$

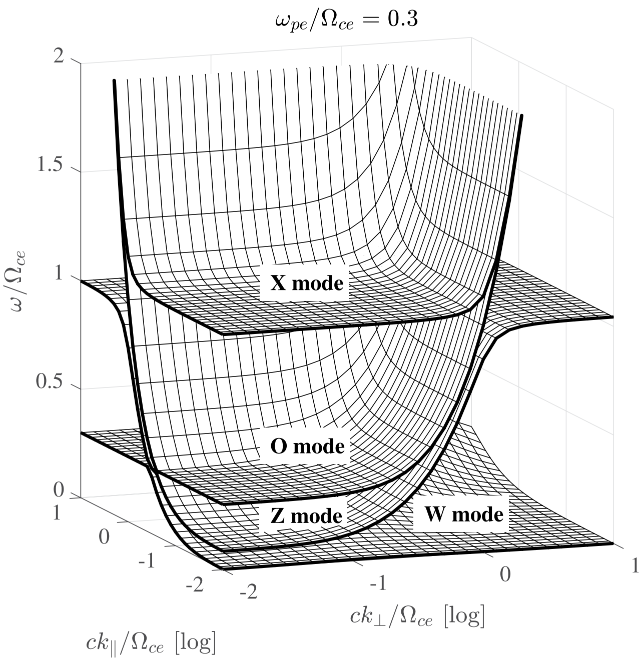

**Figure 7.** Dispersion surfaces for $\omega_{pe}/\Omega_{ce}=f_{pe}/f_{ce}=0.3$ showing the four branches of magnetoionic modes, X, O, Z, and W.

Figure 7 displays the numerical solution of Equation 9 in the format of dispersion surfaces, $w$ versus $q_\perp=q\sin\theta$ and $q_\parallel=q\cos\theta$. The four branches of magnetoionic modes, X, O, Z, and W, are indicated from the highest to the lowest surfaces. For the choice of $r=f_{pe}/f_{ce}=\omega_{pe}/\Omega_{ce}=0.3$ the most important radiation mode (in terms of the relative growth rates for cyclotron maser instability) is the O mode at the fundamental cyclotron frequency $w\sim1$ (or $\omega\sim\Omega_{ce}$). The loss-cone distribution (Equation 4) can also excite Z mode with highly oblique angles of propagation and for short wavelengths, $q_\perp\gg1$. The Z-mode excitation problem is the subject of the next subsection.

For the present O-mode generation we choose the O-mode dispersion surface as input $w$ and proceed to calculate the instantaneous growth rate (Equation 7). The result is plotted in Figure 8 (left). The input parameters are the same as already discussed in relation to the model hot loss-cone distribution, (Equation 4), namely, $r_n=n_h/n_0=10^{-3}$, $\alpha_h=0.3$, $\mu_L=0.95$, $\delta=0.1$, and $\Delta=0$, and additionally, we choose $r=\omega_{pe}/\Omega_{ce}=f_{pe}/f_{ce}=0.3$. As is apparent, the frequency bandwidth associated with the presumed remote O-mode emission is extremely narrow centered around the local gyro frequency. This is the reason why we interpret the O-mode emission detected by Juno as being remotely generated, since the observed O-mode in Figure 2 is close to $f_{pe}$, which is far below $f_{ce}$.

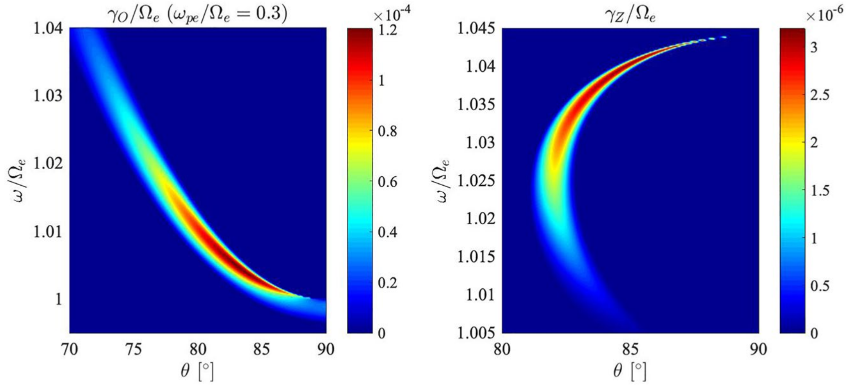

**Figure 8.** Initial O-mode growth rate for $\omega_{pe}/\Omega_{ce} = f_{pe}/f_{ce} = 0.3$ (left) and the same for Z-mode (right). The magnitudes of normalized O- and Z-mode growth rates, $\gamma_O/\Omega_{ce}$ and $\gamma_Z/\Omega_{ce}$, are represented by the color map scheme, and indicated in the color bars. The format of the growth rate plot is normalized frequency, $\omega/\Omega_{ce}$, versus the propagation angle, $\theta$ (°).

As discussed in Yoon et al. (2021) and in Yoon and Ziebell (1995), Ziebell and Yoon (1995), the time evolution of the electron distribution function and the self-consistently excited waves (in this case, O mode) can be studied effectively by employing the reduced quasilinear theory. The method involves taking the quasilinear kinetic equation and the assumption that the time evolution of the electron distribution function only involves the adiabatic change in $\Delta$, while the basic form of distribution function is given by Equation 4. Then, the dynamical equation for $\Delta$ can be deduced from the quasilinear particle kinetic equation by taking an appropriate velocity moment of the equation. As in Yoon et al. (2021), we take the moment $\int d\mathbf{u}\mu^2 f_h$. For the sake of brevity, we omit the intermediate steps (as they closely follow Yoon and Ziebell (1995), Ziebell and Yoon (1995), Yoon et al. (2021)), and write down the final form of equation,

$$\begin{aligned}\frac{d\Delta}{dT} &= \frac{12\pi^{1/2}(A+\Delta)}{A-3B}\int d\mathbf{q}\,\frac{W(\mathbf{q})}{(1+K^2)\cos^2\theta+\tau^2}\Bigg(\Theta(1-w)\int_{-1}^{1}d\mu\,\Pi(u_+,\mu)\\ &\quad+\Theta(w-1)\Theta\big(1-\mu_*^2\big)\sum_{+,-}\int_{\mu_*}^{1}d\mu\,\Pi(u_\pm,\mu)\Bigg),\\ \frac{\partial W(\mathbf{q})}{\partial T} &= \Gamma(\mathbf{q})W(\mathbf{q}),\end{aligned} \tag{10}$$

where $\Gamma(\mathbf{q})$ is defined in Equation 7, various quantities are defined as in Equation 8, including the quantity $A$ (see Equation 4), and

$$\begin{aligned}T &= \Omega_{ce}t, \qquad W(\mathbf{q})\,d\mathbf{q} = \frac{\delta E^2(\mathbf{k})\,d\mathbf{k}}{B_0^2},\\ \Pi(u,\mu) &= \left(\frac{1}{w}-1+\mu^2\right)\frac{\mathcal{M}(u,\mu)\mathcal{P}(u,\mu)}{2u^2\left|u\left[q^2\mu^2\cos^2\theta+2(1-w)w\right]^{1/2}\right|},\\ B &= \frac{1}{2}\int_{-1}^{1}d\mu\,\mu^2\left(\tanh\frac{\mu+\mu_L}{\delta}-\tanh\frac{\mu-\mu_L}{\delta}\right).\end{aligned} \tag{11}$$

We have solved this set of equations and the result is summarized in Figure 9. Plotted in the top-left and bottom-left panels, respectively, are the initial ($t = 0$) and final ($T = \Omega_{ce}t = 10^3$) loss-cone distributions, respectively. Although we have not actually solved the quasilinear kinetic equation numerically but rather, we have only solved for the time evolution of $\Delta$, we can nevertheless, reconstruct the velocity space distribution function since we assumed that the basic mathematical form (Equation 4) is maintained at every time step. This is, of course, an approximation, but since the loss-cone is the free energy source for the instability, it is reasonable to assume that the primary effect of pitch-angle diffusion is to erode the loss-cone boundary and fill up the empty loss cone. Top-right and bottom-right panels, respectively, depict the time evolution of the loss-cone filling parameter $\Delta$, which grows from its initial value of zero to ~45 at saturation, and the integrated wave energy density associated with the O-mode, $\int d\mathbf{k}W(\mathbf{k})$. Note that the O-mode, while the saturation level is quite low, is nevertheless quite effective in pitch-angle scattering such that at the final time step, the initial loss-cone feature has almost disappeared. As it will be discussed next, the Z-mode is not as effective in reducing the loss-cone feature.

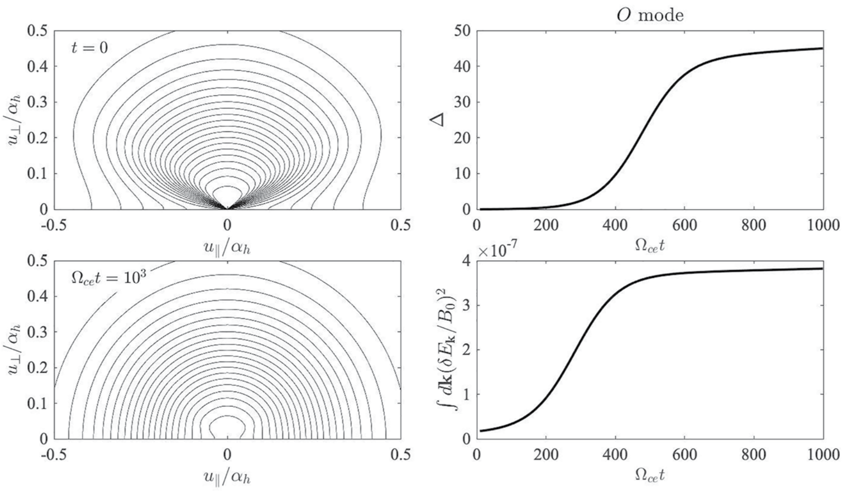

**Figure 9.** Quasilinear wave and particle analysis based on the reduced method as exemplified by the velocity moment kinetic equation $d\Delta/dt$ (Equation 10). Top-left and bottom-left panels, respectively, display the initial and final loss-cone distribution. Top-right and bottom-right panels depict the time evolution of the loss-cone fill parameter $\Delta$, and the integrated wave energy density associated with the O-mode. Note that the O-mode, while the saturation amplitude is quite low, is nevertheless quite effective in pitch-angle scattering such that at the final time step, the initial loss-cone feature has almost disappeared.

We note that the quasilinear analysis presented here pertains to a presumed remote O-mode source region. In order to provide a plausible explanation for the observation, one must quantify the propagation of O- and Z-modes to the vicinity of Juno spacecraft by implementing the wave propagation through an inhomogeneous medium. Before we discuss such a scheme, we next consider a presumed remote Z-mode source and the related quasilinear property of Z-mode evolution.

## 5.2. Quasilinear Analysis of Z-Mode in the Source Region

Linear and quasilinear analysis of Z-mode in the remote source region can be done in an analogous manner: The instantaneous Z-mode growth rate is given by the same formula as in Equation 7, except that the following quantities replace the prior definitions:

$$\mathcal{M}(u,\mu) = \left\{ \left( \tau w K \sin\theta - w \sin^2\theta + 1 \right) [J_0(b) + J_2(b)] - \tau [J_0(b) - J_2(b)] \right\}^2,$$
$$K = \frac{r^2}{r^2 - w^2} \frac{\sin\theta}{w + \tau}, \qquad R = 1 + \frac{r^2}{w^2} \frac{\tau^2 w^2 - r^2 \cos^2\theta}{(w+\tau)^2 \sin^2\theta} \frac{\tau^2 - \cos^2\theta}{\tau^2 + \cos^2\theta}. \tag{12}$$

The initial Z-mode growth rate is plotted in Figure 8 (right). To calculate the Z-mode rate we chose the third dispersion surface from top in Figure 7 as the desired $w$, which corresponds to the Z mode. The input parameters are the same before. Again, the frequency range for the presumed remote Z-mode source region is extremely narrow centered around the local gyro frequency. In contrast, the Z-mode emission detected by Juno has a broad frequency range bounded from below by $f_Z$, but apparently broadly emitted beyond $f_{pe}$, and presumably all the way up to the resonance frequency, which is obscured by the strong O-mode emission close to $f_{pe}$.

We have carried out the quasilinear analysis as in the case of O-mode, except that we now assume that only the Z-mode is excited in the remote source. The result is summarized in Figure 10. The main difference with the O mode is that the Z-mode saturates quite early when compared with the O-mode. Despite the fact that the initial Z-mode growth rate is lower in magnitude in comparison with the O mode, the Z mode reaches higher saturation intensity than the O mode. This type of nonlinear behavior could not be predicted by linear theory alone, which shows why quasilinear analysis is necessary and useful. It is interesting to note that the Z mode is somewhat less effective in pitch-angle scattering of electrons. This can be seen by the relatively low saturation value of $\Delta$, which

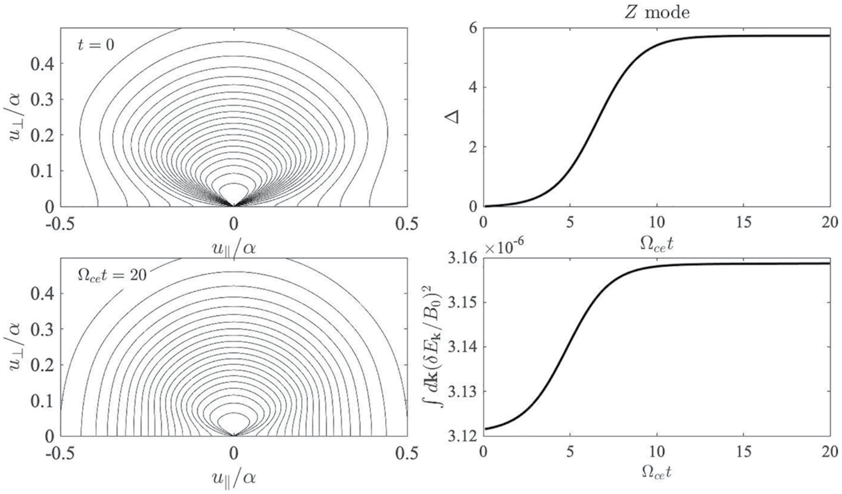

**Figure 10.** The same as Figure 9, except that the quasilinear wave and particle analysis is based on the Z-mode excitation and saturation. Note that while the Z-mode saturates quite early when compared with the O-mode, and it is somewhat ineffective in pitch-angle scattering such that an appreciable loss-cone feature remains at the saturation.

translates to the fact that an appreciable loss-cone feature remains in the reconstructed velocity distribution function at the saturation (as can be seen in the bottom-left panel of Figure 10).

### 5.3. Propagation to the Local Observation Sites

Having discussed the properties of O- and Z-modes at the source regions, which are supposedly located in regions away from the observation site, we now discuss a simple scheme to implement the propagation of the remotely-generated waves through inhomogeneous medium. Ideally, the wave propagation in spatially-varying medium must be discussed with a Wentzel-Kramers-Brillouin (WKB) type of wave analysis that takes into account the group velocity, and the divergence of wave intensity along the ray paths, etc. Such a first-principle approach is clearly beyond the scope of the present analysis. Instead, we take a rather heuristic approach. We consider that the wave spectra generated at their respective sources propagate to the observation site without experiencing a significant loss of the wave power by absorption along the propagation trajectory, or suffering any sizable reduction in the wave intensity by the divergence of ray paths. We simply view the problem as if the medium is adiabatically varying in time. That is, we conceive of a hypothetical observer moving along the ray and experiencing slowly varying local magnetic field intensity and ambient density, while the wave intensity remains quasi constant. In such a scheme, a simple way to implement this idea is to allow the magnetic field intensity to slowly vary, thus the cyclotron frequency varies from its initial value to its final value,

$$\Omega_{ce}(0) \rightarrow \Omega_{ce}(0) f_B, \tag{13}$$

where $f_B$ is factor that determines how the local magnetic field intensity scales. Given that the remotely generated O- and Z-modes have frequencies close to $\Omega_{ce}(0)$, and that the observed frequencies at the location of Juno satellite are much lower than local $f_{ce}$, we determine that $f_B$ must be much higher than unity. While the magnetic field intensity undergoes adiabatic change, the ambient density must also vary. In the previous two subsections on the remote wave growths we adopted $f_{pe}(0)/f_{ce}(0) = 0.3$, which could be true for a source region near the inner edge of the Io torus. The Juno observations, on the other hand, are characterized by the frequency ratio $(f_{pe}/f_{ce})_{\text{obs}} \sim 0.142$—see Figures 1 and 2 and discussions thereof. We model the dependence of the frequency ratio as

$$\frac{f_{pe}}{f_{ce}} = \frac{r(0) + r_{\text{obs}}\left(f_B^2 - 1\right)}{f_B^2}, \tag{14}$$

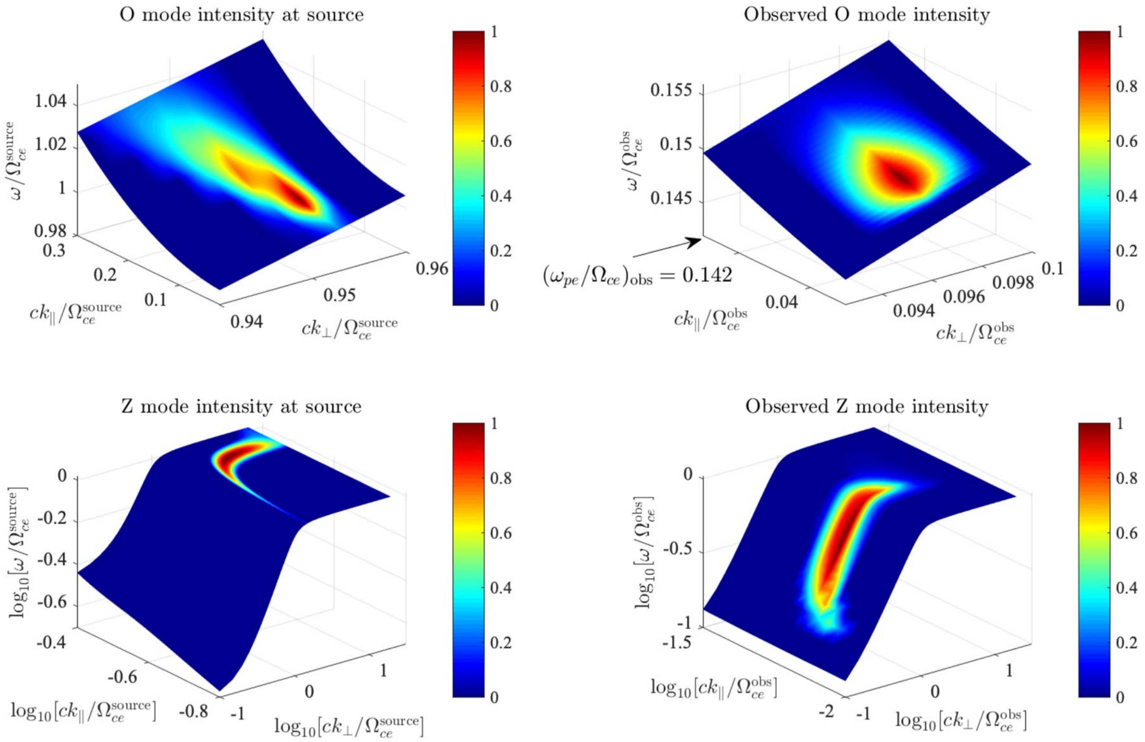

**Figure 11.** The left-hand panels depict the O- and Z-mode saturated wave intensities (top and bottom, respectively) at their respective sources. The right-hand panels correspond to the same spectra when ($\omega$, $\mathbf{k}$) are scaled by ($\omega/f_B$, $\mathbf{k}/f_B$) with $f_B = 10$, and also by rescaling $\left(\omega_{pe}/\Omega_{ce}\right)_{\mathrm{source}} = 0.3$ to $\left(\omega_{pe}/\Omega_{ce}\right)_{\mathrm{obs}} = 0.142$.

where $r(0) = f_{pe}(0)/f_{ce}(0) = 0.3$ and $r_{\mathrm{obs}} = (f_{pe}/f_{ce})_{\mathrm{obs}} \sim 0.142$, so that if $f_B = 1$, then we have $r = r(0)$, while for $f_B \gg 1$, we have $r = r_{\mathrm{obs}}$. With this scheme, the wave intensity, $W(\mathbf{q}) = |\delta E^2(\mathbf{k})|/B_0^2$, simply scales as

$$W(\mathbf{q}) \rightarrow W(\mathbf{q}/f_B), \tag{15}$$

since the normalized wave vector scales inversely with respect to $f_B$ via $\mathbf{q} = c\mathbf{k}/(\Omega_{ce} f_B)$. With such a simple scaling, we plot the initial and final wave spectra for O- and Z-modes versus the local wave numbers, while also rescaling the normalized wave frequency, $w \rightarrow w/f_B$. In plotting the "final" state we chose $f_B = 10$.

The result is plotted in Figure 11. In the top-left panel we display the saturated O mode intensity computed by solving the set of self-consistent quasilinear equations. The format is the O-mode dispersion surface with the wave intensity superposed. To aid the visualization, we have made use of the color map to indicate the normalized wave intensities. The color scheme represents the normalization with respect to the maximum intensity. Thus, the dark red, which represents the maximum intensity, is unity, while the blue background represents the minimum (~0) intensity. In this manner, the local excitation wave frequency at the source can clearly be seen to be in the close vicinity of the electron gyro frequency. On the top-right, we plot the O-mode spectrum at the observation site, where both the wave vector and frequency are inversely scaled with $f_B$. We have also indicated the observed frequency ratio, $r_{\mathrm{obs}} = 0.142$, which indicates that the O-mode that has propagated from the source region is now very close but higher than the cutoff value. Notice how the O-mode frequency is substantially lower than the electron gyro frequency at the satellite location. These features are consistent with observations (Figures 1 and 2). We have also repeated the same plots in the bottom left- and right panels for Z-mode. At the source, the Z-mode excitation is similarly characterized by emission in the close vicinity of the gyro-frequency, but in the vicinity of the Juno satellite, the Z-mode spectrum has turned into a broadband pattern that spans a wide swath of frequencies close to the lower cutoff $f_Z$ and extending to the resonance, $f_Z^{\mathrm{res}}$. Again, this feature is consistent with observations.

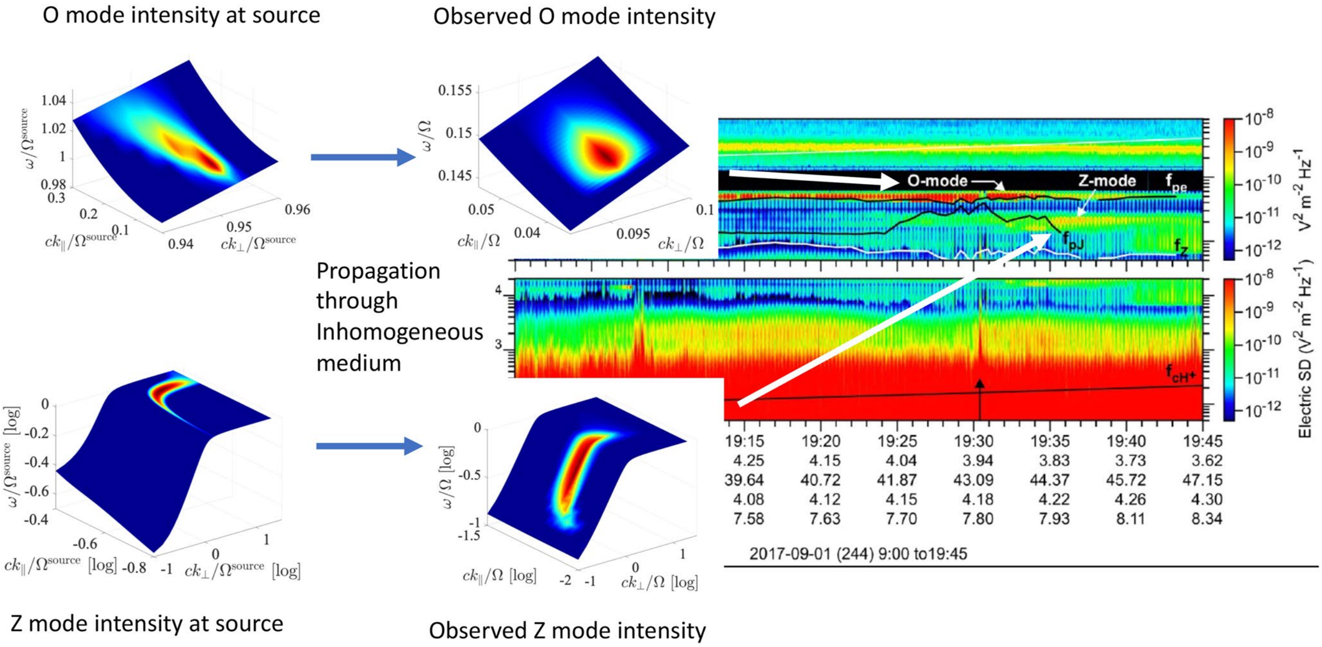

**Figure 12.** Summary of the present paper: (Left) The remotely-generated and O- and Z-modes. (Middle) Propagation through the inhomogeneous medium, which turns O-mode spectrum to be close to local $f_{pe}$, and Z-mode spectrum to be broadband. (Right) Arrows indicating that our interpretation is consistent with observation.

## 6. Summary

In this work we have presented observations of plasma and wave data obtained by the Juno spacecraft in orbit about Jupiter. Intense Z-mode and O-mode emission, among the highest observed for Z-mode in the Jovian magnetosphere, are identified in a low to mid-latitude region near the inner edge of the Io torus. There is a possibility of inferred field-aligned bursty electrons, which lead to broad-banded electrostatic emission seen present at times in the observations (near the arrows in the bottom panel of Figure 2). However, pitch angles less than ~5° were not sampled during the time of the observations by either JADE or JEDI to confirm this.

Menietti et al. (2020) and Menietti et al. (2021) reported a survey of Z-mode emission at Jupiter at middle latitudes in the region near and inward of $M \sim 10$, with intensities that are about 50 times the magnitude of those previously observed at Saturn. Z-mode at Saturn is believed to potentially accelerate electrons to MeV energies in the region inside the orbit of Enceladus through a Doppler-shifted cyclotron resonance (Woodfield et al., 2018). Further, simulations by Yu et al. (2019) indicate that at Saturn the combined effects of equatorial chorus and higher latitude Z-mode can scatter and energize electrons along field lines that map to the radiation zones. The higher intensity Z-mode waves at Jupiter are also observed at larger latitudes and along similar field lines as at Saturn, thus suggesting we may expect similar results at Jupiter.

We have been able to estimate the density of the plasma based on the lower frequency cutoff of the observed Z-mode emission. The results are compatible with the electron density measurements of the JADE plasma instrument after accounting for the absence of cold plasma observations ($E < 50$ eV). We have also used the measured PSD of the JADE and JEDI instruments to calculate estimated growth rates of the observed O-mode and Z-mode emission assuming a loss cone instability and quasilinear wave analysis (Yoon et al., 2021). The averaging times of the electron phase space samples are large (30 s), and the measured distributions for both the O-mode and Z-mode are likely in a relaxed state. The calculated growth rates do not match the observed frequency range for either the O or Z modes. It is likely that the source region of each of these wave modes is more remote, perhaps near the outer edges of the Io torus.

To summarize our findings, we present in Figure 12, a graphical compilation of the present finding. On the left (top and bottom) are the remotely-generated and O- and Z-mode spectra, respectively, which are recapitulations of Figure 11 left panels (top and bottom). As already noted, these have spectra with peaks in the vicinities of remote electron gyro frequencies. By implementing a simple scheme to characterize the propagation through the inhomogeneous medium, these spectra are distorted such that by the time Juno detects these waves, the O-mode spectrum has peak frequency close to local $f_{pe}$, while the Z-mode spectrum has turned into a broadband mode with frequency ranging from the Z-mode cutoff at low end, and extending to the Z-mode resonance at high end (which is partially occulted by the O-mode emission). This is depicted in the middle panels (again, these are recapitulations of Figure 11 right panels). Finally, on the right, we partially reproduce Figure 2, with arrows indicating the correspondence between the theoretical O- and Z-mode spectra and the observation.

Quasilinear (QL) analysis allows us to hypothesize that the O-mode and Z-mode emission observed by Juno was generated nearby in a region of lower $f_{ce}$ and higher $f_{pe}$. From the direction finding results, this could possibly be regions in the nearby inner edge of the plasma torus. Figure 1a of Imai et al. (2017) shows contours of $f_{RX}$ (lower cutoff of right-hand polarized extraordinary mode radio emission) and $f_{LO} = f_z$. We hypothesize the source region for the O-mode and Z-mode might be near the inner and outer edges of the Io torus depicted in this figure. The observations and QL analysis provide a unique opportunity to confirm both the wave modes of intense O and Z mode in the inner and outer Jovian magnetosphere, but also provide a convincing theoretical description of the possible development of the waves in space and time.

While the lack of sufficient resolution handicapped the analysis to confirm source regions for the O and Z-mode, the data nevertheless provide an excellent and rare opportunity to confirm identification of intense Z and O-mode waves in the inner region of the Jovian magnetosphere in a region with magnetic field lines that can map to the radiation belts. There is evidence that the O-mode and Z-mode emissions are at times mixed, which has been speculated in the past, but not confirmed. The importance of Z-mode in accelerating electrons as reported in the inner Saturn magnetosphere (Woodfield et al., 2018; Yu et al., 2019) makes these new wave mode confirmations at Jupiter of particular interest.

## Data Availability Statement

Juno Waves data used in the generation of the figures of this work are located at NASA Planetary Data System website, https://pds-ppi.igpp.ucla.edu/data/JNO-E_J_SS-WAV-3-CDR-SRVFULL-V2.0. JEDI calibrated data are located at https://pds-ppi.igpp.ucla.edu/data/JNO-J-JED-3-CDR-V1.0/. The MAG calibrated data are located at https://pds-ppi.igpp.ucla.edu/data/JNO-SS-3-FGM-CAL-V1.0/ and at https://pds-ppi.igpp.ucla.edu/data/JNO-J-3-FGM-CAL-V1.0. The over-plotted data used to generate Figure 2 of this article, as well as the data used to generate Figures 4 and 6, can be found in tabular form at https://doi.org/10.5281/zenodo.7373638.
The theoretical plots are in normalized units, and the equations are clearly explained in the text. Therefore, no actual data are generated by the theory.

**Acknowledgments**

The authors wish to thank K. Kurth for clerical assistance and J. Chrisinger for help with the figures. JDM acknowledges support from NASA Grant 80NSSC19K1262. P. H. Y. was supported by NSF Grant 2203321, NASA Grant 80NSSC23K0662, and the Department of Energy (DOE DE-SC0022963) through the NSF/DOE Partnership in Basic Plasma Science and Engineering. Research conducted at the University of Iowa was supported by NASA New Frontiers Program through Contract 699041X with Southwest Research Institute. P. K. and F. A. were funded by NASA New Frontiers Program for Juno (for P. K. this was through a subcontract with Southwest Research Institute). We acknowledge the use of the Space Physics Data Repository at the University of Iowa supported by the Roy J. Carver Charitable Trust.

## References

Allegrini, F., Bagenal, F., Bolton, S., Connerney, J., Clark, G., Ebert, R. W., et al. (2017). Electron beams and loss cones in the auroral regions of Jupiter. *Geophysical Research Letters*, *44*(14), 7131–7139. https://doi.org/10.1002/2017GL073180

Allegrini, F., Mauk, B., Clark, G., Gladstone, G. R., Hue, V., Kurth, W. S., et al. (2020). Energy flux and characteristic energy of electrons over Jupiter's main auroral emission. *Journal of Geophysical Research: Space Physics*, *125*(4), e2019JA027693. https://doi.org/10.1029/2019JA027693

Bevington, P. R. (1969). *Data reduction and error analysis for the physical sciences* (pp. 235–242). McGraw-Hill Book Company.

Bolton, S. J., Thorne, R. M., Gurnett, D. A., Kurth, W. S., & Williams, D. J. (1997). Enhanced-whistler-mode emissions: Signatures of interchange motion in the Io torus. *Geophysical Research Letters*, *24*(17), 2123–2126. https://doi.org/10.1029/97GL02020

Carr, T. D., Desch, M. D., & Alexander, J. K. (1983). Phenomenology of magneospheric radio emissions. In A. J. Dessler (Ed.), *Physics of the Jovian magnetosphere* (p. 226). Cambridge University Press.

Connerney, J. E. P., Kotsiaros, S., Oliversen, R. J., Espley, J. R., Joergensen, J. L., Joergensen, P. S., et al. (2018). A new model of Jupiter's magnetic field from Juno's first nine orbits. *Geophysical Research Letters*, *45*(6), 2590–2596. https://doi.org/10.1002/2018GL077312

Elliott, S. S., Sulaiman, A. H., Kurth, W. S., Faden, J., Allegrini, F., Valek, P. W., et al. (2021). The high-latitude extension of Jupiter's Io torus: Electron densities measured by Juno/Waves. *Journal of Geophysical Research: Space Physics*, *126*(8), e2021JA029195. https://doi.org/10.1029/2021JA029195

Gu, X., Thorne, R. M., Ni, B., & Ye, S.-Y. (2013). Resonant diffusion of energetic electrons by narrowband Z mode waves in Saturn's inner magnetosphere. *Geophysical Research Letters*, *40*(2), 255–261. https://doi.org/10.1029/2012GL054330

Gurnett, D. A., & Frank, L. A. (1972). ELF noise bands associated with auroral electron precipitation. *Journal of Geophysical Research*, *77*(19), 3411–3417. https://doi.org/10.1029/JA077i019p03411

Horne, R. B., & Thorne, R. M. (1998). Potential waves for relativistic electron scattering and stochastic acceleration during magnetic storms. *Geophysical Research Letters*, *25*(15), 3011–3014. https://doi.org/10.1029/98GL01002

Imai, M., Kurth, W. S., Hospodarsky, G. B., Bolton, S. J., Connerney, J. E. P., & Levin, S. M. (2017). Direction-finding measurements of Jovian low-frequency radio components by Juno Waves instrument near Perijove 1. *Geophysical Research Letters*, *44*(13), 6508–6516. https://doi.org/10.1002/2017GL072850

Kollmann, P., Roussos, E., Paranicas, C., Woodfield, E. E., Mauk, B. H., Clark, G., et al. (2018). Electron acceleration to MeV energies at Jupiter and Saturn. *Journal of Geophysical Research: Space Physics*, *123*(11), 9110–9129. https://doi.org/10.1029/2018JA025665

Kurth, W. S., Hospodarsky, G. B., Kirchner, D. L., Mokrzycki, B. T., Averkamp, T. F., Robison, W. T., et al. (2017). The Juno waves investigation. *Space Science Reviews*, *213*(1–4), 347–392. https://doi.org/10.1007/s11214-017-0396-y

Lyons, L. R., Throne, R. M., & Kennel, C. F. (1972). Pitch-angle diffusion of radiation belt electrons within the plasmasphere. *Journal of Geophysical Research*, *77*(19), 3455–3474. https://doi.org/10.1029/JA077i019p03455

Mauk, B. H., Haggerty, D. K., Jaskulek, S. E., Schlemm, C. E., Brown, L. E., Cooper, S. A., et al. (2017). The Jupiter Energetic Particle Detector Instrument (JEDI) investigation for the Juno mis-sion. *Space Science Reviews*, *213*(1–4), 289–346. https://doi.org/10.1007/s11214-013-0025-3

Mauk, B. H., Williams, D. J., McEntire, R. W., Khurana, K. K., & Roederer, J. G. (1999). Storm-like dynamics of Jupiter's inner and middle magnetosphere. *Journal of Geophysical Research*, *104*(A10), 22759–22778. https://doi.org/10.1029/1999JA900097

McComas, D. J., Alexander, N., Allegrini, F., Bagenal, F., Beebe, C., Clark, G., et al. (2017). The Jovian Auroral Distributions Experiment (JADE) on the Juno mission to Jupiter. *Space Science Reviews*, *213*(1–4), 547–643. https://doi.org/10.1007/s11214-013-9990-9

Melrose, D. B. (1986). *Instabilities in space and laboratory plasmas* (pp. 170–171). Cambridge University Press.

Menietti, J. D., Averkamp, T. F., Imai, M., Kurth, W. S., Clark, G. B., Allegrini, F., et al. (2020). Low-latitude whistler-mode and higher-latitude Z-mode emission at Jupiter observed by Juno. *Journal of Geophysical Research: Space Physics*, *126*(2), e2020JA028742. https://doi.org/10.1029/2020JA028742

Menietti, J. D., Averkamp, T. F., Kurth, W. S., Imai, M., Faden, J. B., Hospodarsky, G. B., et al. (2021). Analysis of whistler-mode and Z-mode emission in the Juno primary mission. *Journal of Geophysical Research: Space Physics*, *126*(11), e2021JA029885. https://doi.org/10.1029/2021JA029885

Menietti, J. D., Averkamp, T. F., Ye, S.-Y., Persoon, A. M., Morooka, M. W., Groene, J. B., & Kurth, W. S. (2018). Extended survey of Saturn Z-Mode wave intensity through Cassini's final orbits. *Geophysical Research Letters*, *45*(15), 7330–7336. https://doi.org/10.1029/2018GL079287

Menietti, J. D., Yoon, P. H., Pisa, D., Averkamp, T. F., Sulaiman, A. H., Kurth, W. S., et al. (2019). The role of intense upper hybrid resonance emissions in the generation of Saturn narrowband emission. *Journal of Geophysical Research: Space Physics*, *124*(7), 5709–5718. https://doi.org/10.1029/2019JA026855

Menietti, J. D., Yoon, P. H., Písa, D., Ye, S.-Y., Santolík, O., Arridge, C. S., et al. (2016). Source region and growth analysis of narrowband Z-mode emission at Saturn. *Journal of Geophysical Research: Space Physics*, *121*(12), 11929–11942. https://doi.org/10.1002/2016JA022913

Sulaiman, A. H., Elliott, S. S., Kurth, W. S., Faden, J. B., Hospodarsky, G. B., & Menietti, J. D. (2021). Inferring Jovian electron densities using plasma wave spectra obtained by the Juno/Waves instrument. *Journal of Geophysical Research: Space Physics*, *126*(8), e2021JA029263. https://doi.org/10.1029/2021JA029263

Thorne, R. M., Armstrong, T. P., Stone, S., Williams, D. J., McEntire, R. W., Bolton, S. J., et al. (1997). Galileo evidence for rapid interchange transport in the Io torus. *Geophysical Research Letters*, *24*(17), 2131–2134. https://doi.org/10.1029/97GL01788

Treumann, R. A., & Baumjohann, W. (1997). *Advanced space plasma physics*. Imperial College Press. https://doi.org/10.1142/p020

Woodfield, E. E., Horne, R. B., Glauert, S. A., Menietti, J. D., Shprits, Y. Y., & Kurth, W. S. (2018). Formation of electron radiation belts at Saturn by Z-mode wave acceleration. *Nature Communications*, *9*(1), 5062. https://doi.org/10.1038/s41467-018-07549-4

Yoon, P. H., Menietti, J. D., Kurth, W. S., Allegrini, F., & Bolton, S. J. (2021). Quasilinear model of Jovian whistler mode emission. *Journal of Geophysical Research: Space Physics*, *126*(12), e2021JA029930. https://doi.org/10.1029/2021JA029930

Yoon, P. H., Weatherwax, A. T., & Rosenberg, T. J. (1998). On the generation of auroral radio emissions at harmonics of the lower ionospheric electron cyclotron frequency: *X, O* and *Z* mode maser calculations. *Journal of Geophysical Research: Space Physics*, *103*(A3), 4071–4078. https://doi.org/10.1029/97JA03526

Yoon, P. H., & Ziebell, L. F. (1995). Quasilinear evolution of cyclotron maser instability. *Physical Review E*, *51*(5), 4908–4916. https://doi.org/10.1103/PhysRevE.51.4908

Yu, J., Li, L. Y., Cui, J., Cao, J. B., & Wang, J. (2019). Combined effects of equatorial chorus waves and high-latitude Z-mode waves on Saturn's radiation belt electrons. *Geophysical Research Letters*, *46*(15), 8624–8632. https://doi.org/10.1029/2019GL084004

Ziebell, L. F., & Yoon, P. H. (1995). Quasilinear analysis of loss-cone driven weakly relativistic electron cyclotron maser instability. *Physics of Plasmas*, *2*(4), 1285–1295. https://doi.org/10.1063/1.871459